Effect of V microalloying and intercritical annealing on improving strength- ductility balance of Al-bearing medium Mn steel

Cansheng Yu[1,2,a,†], Guo Yuan[1,b], Weisen Zheng[3,c], Yanlin He[3,d], Jian Kang[1,e] and Zhiyuan Chang[2,f]

[1]*State Key Laboratory of Rolling and Automation, Northeastern University, Shenyang 110819, China*

[2]*State Key Laboratory of Vanadium and Titanium Resources Comprehensive Utilization., Pangang Group Research Institute Co., Ltd., Panzhihua Sichuan 617000, China*

[3]*State Key Laboratory of Advanced Special Steel, School of Materials Science and Engineering, Shanghai University, Shanghai 200444, China*

Email: [a]yiyycs@pzhsteel.com.cn, [b]yuanguo@ral.edu.cn, [c]wszheng@shu.edu.cn, [d]ylhe@shu.edu.cn, [e]jikang@ral.edu.cn, [f]yjyczy@pzhsteel.com.cn

The microstructure and mechanical properties of vanadium micro-alloyed Al-bearing medium-Mn steel were studied by SEM, TEM and EBSD technique. The results show that the microstructure of the steel after intercritical annealing from 710℃ to 770℃ was composed of banded δ-ferrite(δ-F), α-ferrite(F) and retained austenite (RA). The mechanical properties of experimental steel mainly depended on the sustained TRIP effect providing of RA during deformation. The large amount of RA and appropriate stability make a significant contribution to the excellent mechanical properties of steel through TRIP effect. With the increase of intercritical annealing temperature, the weakening of TRIP effect and the formation of fresh martensite led to an increase in ultimate tensile strength (UTS), but total elongation (TEL) and product of strength and elongation (PSE) decreased. Vanadium improved the yield strength (YS) and UTS of experimental steel by refining grains and precipitation strengthening, but deteriorated its plasticity. A high V content will lead to a decrease in RA content and stability, weakening the TRIP effect and resulting in a weaker strength-ductility balance. The experimental steel with 0.04% V has excellent comprehensive properties after intercritical annealing at 730℃，maintaining an UTS of 1000 MPa while exhibiting a TEL of 37% and a PSE of 37.7 GPa·%.

Keywords： Vanadium micro-alloying; Aluminum-bearing medium manganese steel; Retained austenite; TRIP effect.

1. Introduction

With the increasingly prominent issues of energy shortage and environmental pollution, under the constraints of the national "dual carbon" goals, lightweight has become the focus of carbon reduction in the automobile industry. Automobile lightweighting are mainly achieved through the interaction and influence among the three major pathways of material lightweighting, structural lightweighting, and process lightweighting. Compared to optimizing the structure and process of automobiles to achieve lightweighting, the lightweighting effect of reducing material density is more significant [1]. Therefore, obtaining low-density steel with both high strength and high plasticity at low cost has become a major challenge. The Al-bearing medium Mn steel (Fe-Mn-Al-C steel) is a promising class of monolithic low density steels that offers a combination of outstanding mechanical properties [2-5], The microstructure of Al-bearing medium Mn steel is mainly

Y. Zhang and M. Ma (eds.), *Proceedings of the 7th International Conference on Advanced High Strength Steel and Press Hardening (ICHSU 2024)*, Atlantis Highlights in Materials Science and Technology 3,
https://doi.org/10.2991/978-94-6463-581-2_37

composed of one or more types of intercritical ferrite (α-F) high-temperature ferrite (δ-F), martensite (M), and retained austenite (RA)[6-10].

RA provides the transformation induced plasticity (TRIP) effect under tensile deformation, which is the key factor for Al-bearing medium Mn steel to achieve excellent strength and plasticity. It's well known that the TRIP effect is sensitive to RA characteristics, such as mechanical stability, size, and the volume fraction[11-14]. The heat treatment of Al-bearing medium Mn steel includes Quenching and Partitioning (Q&P), Quenching-Partitioning-Tempering (Q-P-T), Austenite reverse phase transformation annealing (ART), Among them, ART is the most commonly used. During intercritically annealing(IA) process, martensite transforms into austenite and remains stable at room temperature, achieving excellent strength and plasticity in the steel[15-17]. However, the addition of a large amount of elements such as Al and Mn leads to a serious of problems, such as segregation, hot cracking and so on, resulting in limited progress in industrial practice and commercial applications[18].

The addition of a small amount of microalloying elements (< 0.1%) such as Ti, Nb V or B can cause a remarkable grain refinement[19]. In light of the grain refinement is beneficial to enhance mechanical properties, micro-alloying technology has become an effective way to design a new type of Al-bearing medium Mn steel.

The present study is to develop Al-bearing medium Mn steel with excellent mechanical properties, which is achieved by the combination of vanadium-microalloying technology and the ART process. The research result can provide support for the development of a new generation automotive steel with high strength and high toughness.

2. Experiments

Four 150-kg ingots of Al-bearing medium Mn steels with composition of 0.2C-5Mn-0.25Si-2.20Al-0/0.05/0.10/0.15V (wt.%) were fabricated by vacuum induction melting. The chemical compositions were shown in Table 1. The ingots were forged into rectangular billets (section dimension 30mm × 80mm) after homogenizing at 1250 ℃ for 4 h. The experimental steels were heated to 1230 ℃ and held for 3.5 hours by RX_4-150-14 heating furnace. The homogenized billets were hot rolled from 30mm to 3.5mm. The final rolling temperature was 900 ℃. After hot rolling, the hot-rolled sheet was directly air cooled to room temperature. After removing the oxide scale from the hot-rolled plate through acid pickling, the experimental steels were cold rolled to 1.6mm. Using AccuPyc II 1340 fully automatic true density tester to measure the density of experimental steels. Experimental steels with different vanadium contents were intercritically annealed at 730 ℃ for 3 minutes, and then water quenched to room temperature to explore the effect of vanadium-microalloying on the microstructure and properties of Al-bearing medium Mn steels. B steel was heated to 710 ℃, 730 ℃, 750 ℃, and 770 ℃, and then holding for 3 minutes before being water quenched to room temperature to explore the effect of ART process on the microstructure and properties of Al-bearing medium Mn steels. According to standard GB/T 228-2010, dog-bone-shaped tensile samples of 12.5 mm gauge width and 50 mm gauge length were machined parallel to the rolling direction. The tensile test was performed

at room temperature on an INSTRON 5969 testing machine with a constant 2 mm·min^{-1} cross-head velocity and the data was the average of three samples. The variation process of RA volume fraction with tensile strain was measured using an X-ray stress apparatus with a micro-electronic universal testing. The schematic diagram of the instrument, sample size, and experimental method can refer to Ref. [20].

Table 1. Chemical composition (wt.%) and density(g/cm3) of experimental steel.

Steel	C	Mn	Al	Si	V	N	Density
A	0.21	5.05	2.12	0.26	-	0.002	7.623
B	0.21	4.84	2.30	0.25	0.04	0.002	7.510
C	0.18	4.94	2.30	0.20	0.08	0.003	7.522
D	0.18	5.14	2.19	0.26	0.13	0.003	7.618

The microstructures of the samples were analyzed by Empyrean X-ray diffraction (XRD), Zeiss Sigma 500 field emission scanning electron microscope (SEM) equipped with electron backscattered diffraction (EBSD) and JEM-2100 F transmission electron microscope (TEM). SEM specimens were etched with 4 vol% nitrate alcohol solution after mechanical polishing, while the specimens for XRD and EBSD were electro-polished in a mixed solution of 80% glacial acetic acid and 20% perchloric acid at ~16 V for 2 min. Phase identification and grain characteristics were measured by EBSD, and the acceleration voltage and step size were 20 kV and 0.06 μm, respectively. RA fractions and average C concentration in RA were quantified via XRD (Cu Kα radiation, scan rate of 10°·min^{-1}, diffraction angle (2θ) of 40-100°) based on the integral intensity and austenite lattice parameter of the diffraction peaks. The method can be referred to Refs. [21, 22]. For TEM analysis, thin foil samples with a diameter of 3 mm were mechanically polished to <60 μm, and followed by twin-jet electro-polishing in a mixed solution of 10% perchloric acid and 90% ethanol at -40 °C. The characteristics of precipitates were observed in detail using TEM on carbon extraction replicas.

3. Results and discussion

3.1. *Evolution of microstructure and mechanical properties of V microalloying*

3.1.1. *Microstructure*

Figure 1 presents the SEM images of the microstructure of experimental steels with different vanadium contents intercritical annealed at 730℃. The microstructure constituents of the experimental steels were composed of intercritical ferrite (α-ferrite), banded high-temperature ferrite (δ-ferrite), martensite, and RA. The formation of banded δ- ferrite was mainly due to the addition of Al element, which causes the expansion of the high-temperature BCC phase zone to be retained at room temperature, and subsequently forms banded ferrite during the rolling process. After intercritical annealing, α-ferrite, martensite, and RA were mainly composed of lamellar and equiaxed forms. This was mainly because a large amount of deformation energy accumulated after cold deformation.

After intercritical annealing, a part of α-ferrite undergoes recovery and recrystallization, while part of martensite undergoes ART. The δ-ferrite was formed during solidification and was difficult to equiaxation.

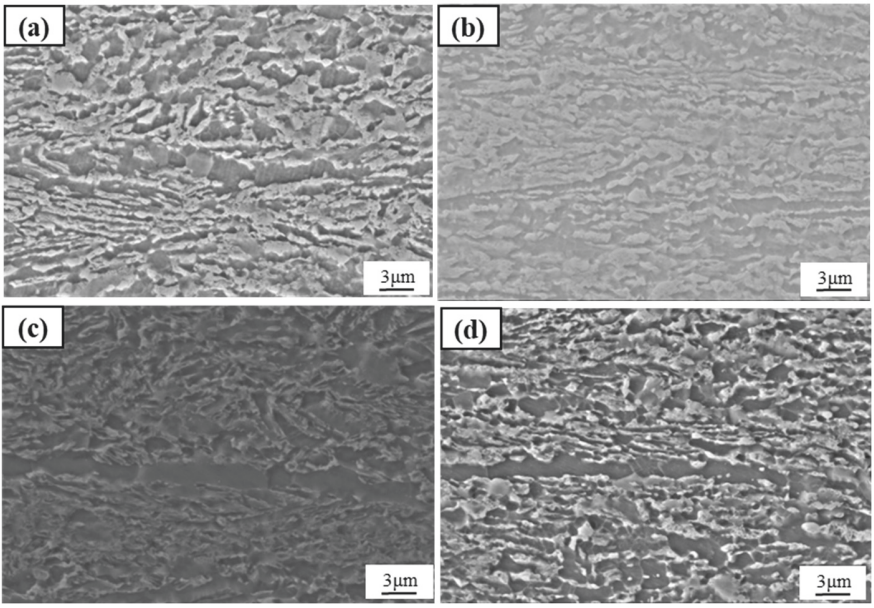

Fig. 1. SEM analysis of microstructure of experimental steels with different V contents after IA at 730 °C: (a) A steel(0V)，(b) B steel (0.04V)，(c) C steel (0.08V)，(d) D steel (0.13V).

Figure 2 presents the EBSD phase map of the microstructure of the experimental steels, where the red area represents BCC structure and the green area represents FCC structure. As shown in the Fig. 2, B steel has the highest RA content, followed by C steel and D steel, while A steel has the lowest RA content. Further analysis of RA content and carbon content were conducted using XRD, and the results showed in Fig. 3. With the addition of vanadium in the experimental steel, the RA slightly decreases, but the RA content in the experimental steels were similar for different vanadium contents. At the same time, the carbon content of RA first increased and then decreased with the increased of vanadium content in the sample, all of them were higher than 1.0 wt.%. The carbon content of B steel (0.04 wt.% V) reaches 1.15 wt.%. This was mainly due to two aspects: 1) The addition of Al can significantly increase the carbon content of RA in the two-phase zone, making the carbon content of RA higher than 1.0 wt.%, which was higher than the carbon content of RA in 0.2C-5Mn steel reported in literature (less than 0.7wt.%). Combined with thermodynamic calculations (Fig. 4), it can be seen that after adding Al to the steel, the carbon content of austenite increased from 0.11wt.% to 0.81 wt.%; 2) The redissolution of VC in B steel further enhanced the carbon content of austenite.

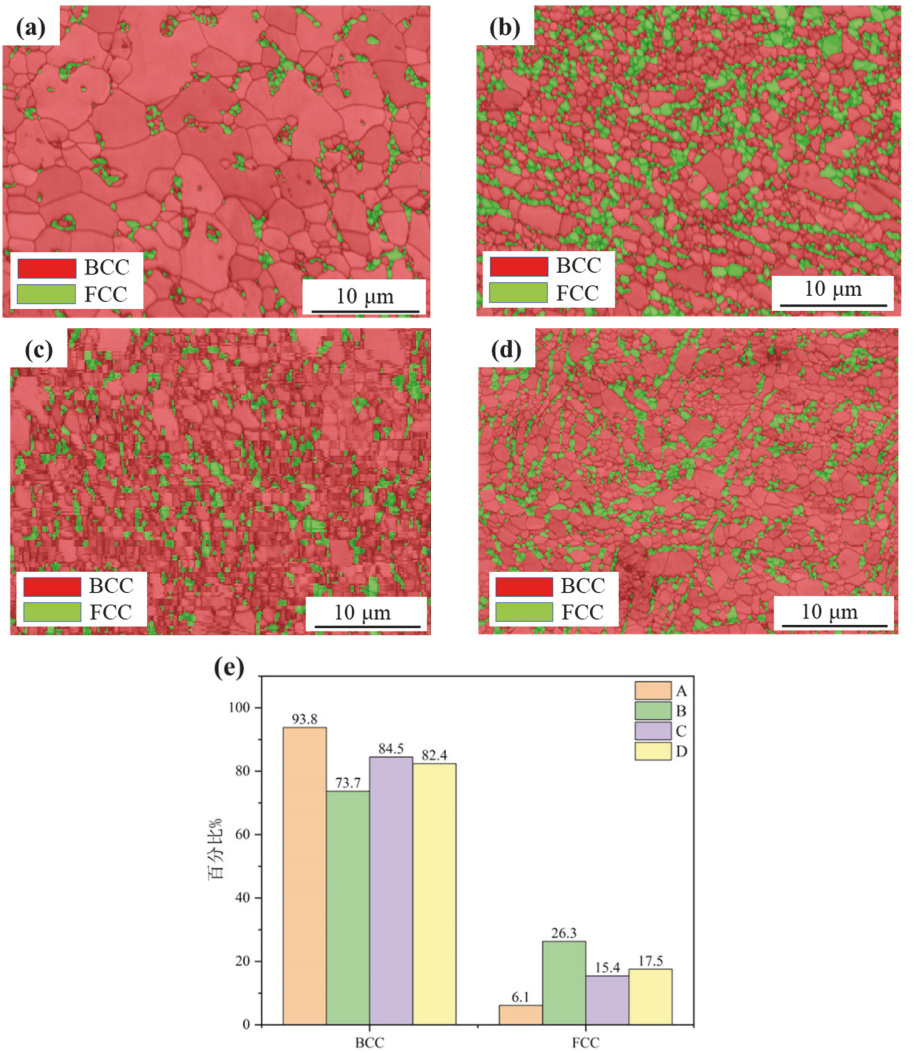

Fig. 2. EBSD phase maps and statistics of experimental steel after intercritical annealing treatment: (a) A steel (0V), (b) B steel (0.04V), (c) C steel (0.08V), (d) D steel (0.13V), (e) Statistics of phase fraction.

Figure 5 shows the IPF maps of the experimental steel microstructure, revealing close orientation of lamellar RA, suggesting predominant nucleation and growth in the martensite lath. The A steel matrix exhibited the largest average size, whereas the B, C, and D steel matrices were refined, demonstrating the effective grain size refinement due to vanadium addition.

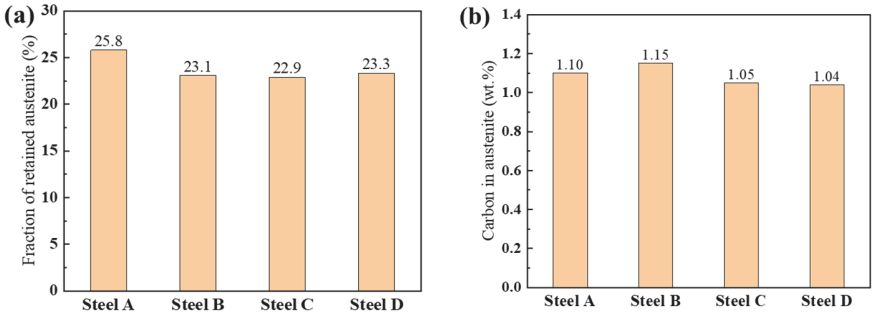

Fig. 3. RA content and carbon content of experimental steel after intercritical annealing treatment

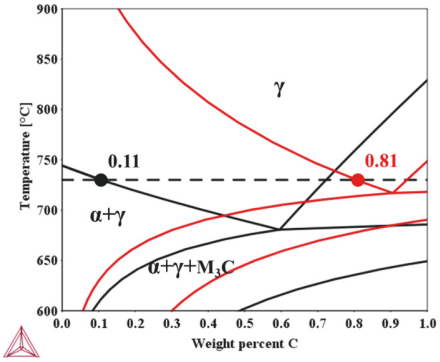

Fig. 4. Vertical cross-sectional phase diagram of aluminum containing and aluminum free steel

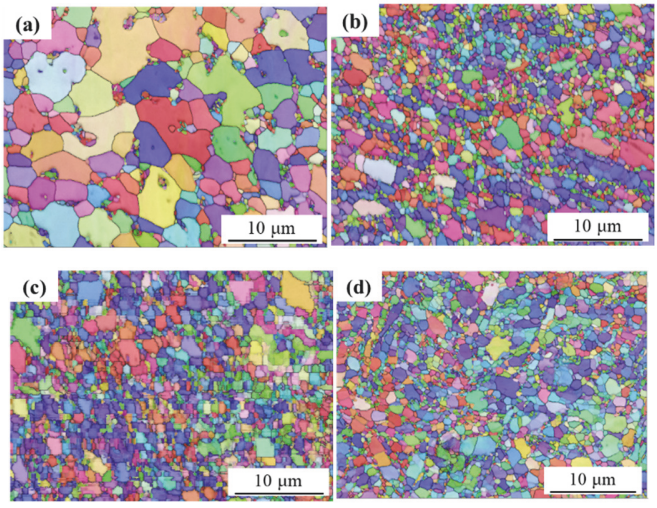

Fig. 5. IPF maps of experimental steel after intercritical annealing treatment: (a) A steel (0V), (b) B steel (0.04V), (c) C steel (0.08V), (d) D steel (0.13V)

Further analysis of the experimental steel's fine structure was conducted using transmission electron microscopy, as depicted in Fig. 6. Bright field images in Fig. 6 (a), (d), (g), and (j) revealed the fine structure, while Figures 6 (b), (e), (h), and (k) displayed dark field images of RA in the steel. Additionally, Fig. 6 (c), (f), (i), and (l) showed selected diffraction patterns of RA in the experimental steels. The RA morphology appeared mainly as lath and block-like structures in the bright field images. STEM-EDS composition analysis indicated that lath austenite formed near ferrite, suggesting nucleation and growth at the martensite lath boundary. Lath-like austenite demonstrated higher mechanical stability than block austenite, contributing to the TRIP effect during tensile deformation and ensuring excellent mechanical properties of the steel. Statistical analysis of austenite grain size revealed average RA sizes of 424nm, 407nm, 395nm, and 403nm for A, B, C, and D steels, respectively. The presence of vanadium resulted in a finer RA size compared to vanadium-free steel.

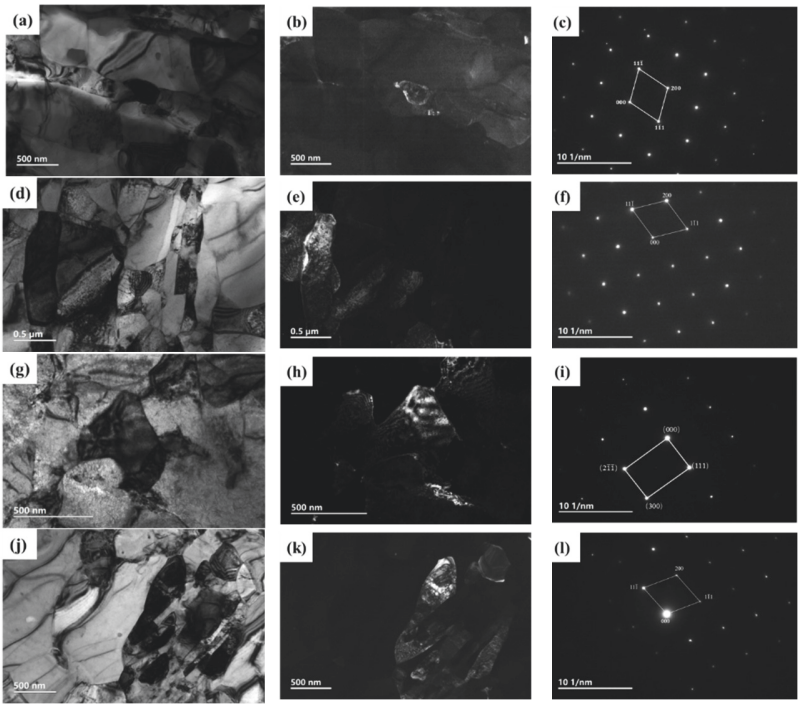

Fig. 6. TEM images of the fine structure of experimental steel after intercritical annealing treatment: (a)~(c) A steel (0V), (d)~(f) B steel (0.04V), (g)~(i) C steel (0.08V), (j)~(l)Dsteel（0.13V）

Fig. 7 (a), (d), and (g) present the bright field images. No second phase was found in A steel, while the second phase were found in B, C, and D steel. Fig. 7 (b), (e), and (h) presented the dark field images of the second phase, and Fig. 7 (c), (f), and (i) presented the selected area electron diffraction (SAED) patterns of the second phase. After calibration of SAED patterns and combining with EDS composition analysis, it can be determined that the second phase in B, C, and D steels were vanadium carbide. From the TEM image, it

can also be seen that vanadium carbide were mainly distributed in the ferrite matrix, with a small amount distributed at the ferrite/austenite interface. EDS was used to perform surface scanning composition analysis on the microstructure of vanadium containing steel (Fig. 7). Vanadium mainly exists in vanadium carbide, and the vanadium content in ferrite and austenite was very low.

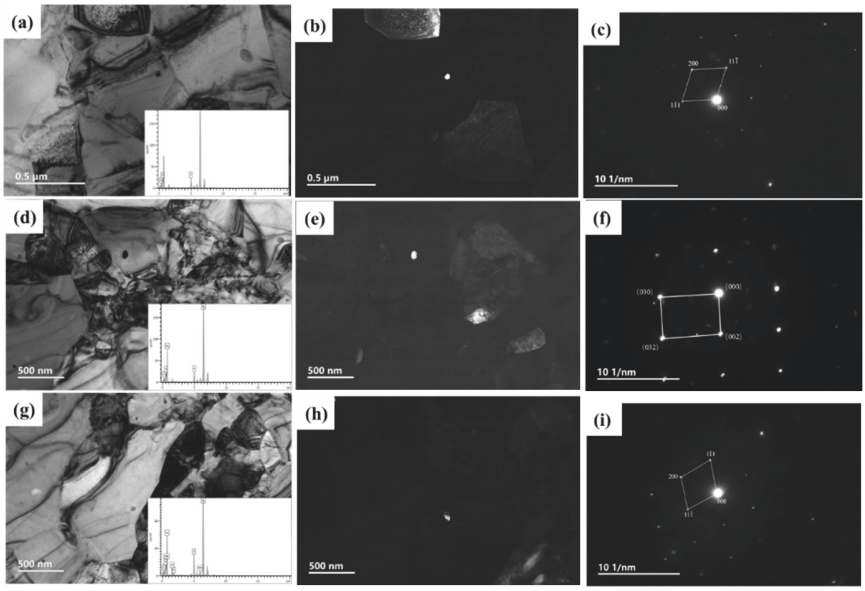

Fig. 7. TEM images of the second phase of vanadium containing steel after critical annealing treatment in the two-phase zone: (a)~(c) B steel (0.04V); (d) ~(f) C steel (0.08V); (g) ~(i) D steel (0.13V)

Figure 8 presented a typical TEM image of a vanadium containing steel extraction sample. It can be seen that the morphology of vanadium carbide was mainly spherical, with a small amount of short rod-shaped particles. The size of vanadium carbide in B steel (0.04V) and C steel (0.08V) decreased from 41.46nm and 55.57nm before the intercritical annealing to 30.01nm and 52.16nm after intercritical annealing, respectively, indicating that vanadium carbide underwent dissolution during the intercritical annealing process. In contrast, the size of vanadium carbide in D steel (0.13V) was increased after intercritical annealing, without any dissolution phenomenon.

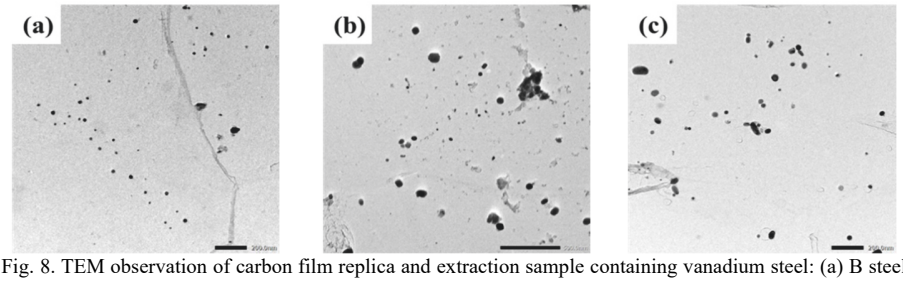

Fig. 8. TEM observation of carbon film replica and extraction sample containing vanadium steel: (a) B steel (0.04V); (b) C steel (0.08V); (c) D steel (0.13V)

Comparing the size distribution of vanadium carbide in B, C, and D steels after intercritical annealing, it was found that the size distribution of vanadium carbide in B steel was concentrated in 10-40nm, mainly composed of smaller particles. The size distribution of vanadium carbide in C steel was mainly in 30-80nm, while the size distribution of vanadium carbide in D steel was mainly in 20-50nm. The size distribution of vanadium carbide in D steel was also relatively wide, with the maximum size reaching 170nm. Overall, the average particle size of vanadium carbide in B steel was smaller than that in C and D steel, indicating that as the vanadium content increases, the particle size of vanadium carbide will also increase. A larger size of vanadium carbide means that more solid solution carbon in the steel will exist in the form of vanadium carbide, resulting in a decrease in the carbon content of austenite and a decrease in its stability.

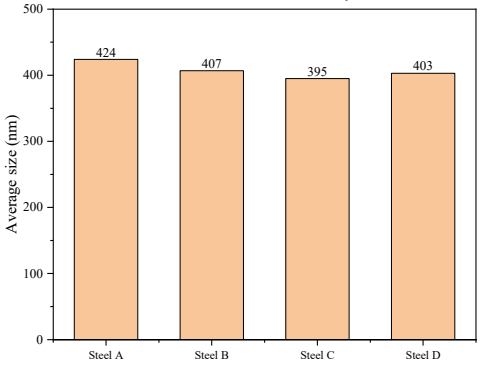

Fig. 9. Average size of vanadium carbide of vanadium carbide in vanadium containing steel before and after IA

3.1.2. *The influence of vanadium on mechanical properties and the stability of austenite*

Figure 10 presented the mechanical properties of experimental steels after intercritical annealing. It can be seen that the UTS of A steel and C steel was lower than 980MPa, while UTS of B steel and D steel was greater than or equal to 980MPa. Among them, B steel had the most excellent mechanical properties, with UTS and TEL reaching 1020MPa and 37.0%, respectively, and product of strength and elongation (PSE) reaching 37.7GPa ·%. The UTS of C and D steel was lower than that of B steel for two reasons: 1) The carbon content of C and D steel were 0.18 wt.%, lower than B steel (0.21 wt.%); 2) The vanadium content in C and D steel were higher than that in B steel, while the formation of vanadium carbide took away solid solution carbon, reduced the stability of RA, and the strengthening effect caused by TRIP effect was lower than that in B steel. In addition, the larger size of vanadium carbide in C steel had an adverse effect on strength.

In terms of elongation after fracture, C steel has the lowest value and A steel has the highest value. The reason for the highest elongation of A steel is that the content of RA is the highest, and there are different morphology of RA, which has the highest stability. Although B steel has the highest carbon content of RA, its TRIP effect is weakened compared to A steel due to a slightly lower RA content, resulting in a slightly lower elongation after fracture of B steel compared to A steel. The RA contents of C steel and D

steel were relatively low, and the carbon content was significantly lower than that of A steel and B steel. This was because excessive vanadium carbide reduced the solid solution carbon of RA, weakens the TRIP effect, and therefore the elongations of C and D steel were lower.

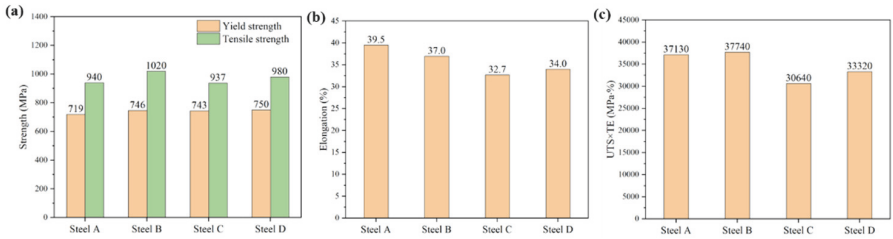

Fig. 10. Tensile properties of experimental steels: (a) yield strength and tensile strength, (b) elongation after fracture, (c) PSE

The determination of RA content in TRIP steel during deformation process was achieved using an X-ray stress meter supplemented by a miniature electronic universal testing machine. After each loading, the volume fraction of RA was measured using an X-ray stress meter. Each point was measured three times and the average value was taken. Fig. 11 presented the stress-strain curve and changed in RA content recorded during the in-situ tensile process of experimental steels after IA. It can be seen that the content of RA in steel A, B, C, and D decreased with increasing strain, and a significant decrease occurs after the yield point, directly confirming the transformation of RA into martensite and strain induced phase transformation. This further indicates that the plasticizing mechanism of the experimental steel was mainly the TRIP effect caused by the transformation of RA to martensite.

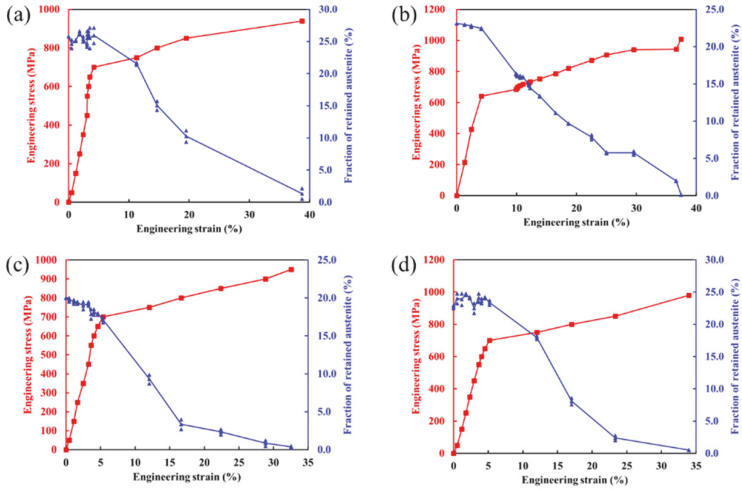

Fig. 11. Changes in RA content with stress-strain curve during in-situ tensile process of experimental steels with different compositions: (a) A steel (0V), (b) B steel (0.04V), (c) C steel (0.08V), (d) D steel (0.13V)

Transmission electron microscopy was used to observe and analyze the tensile samples of B steel, as shown in Fig. 12. Combined with the diffraction pattern, it can be clearly seen that the block like and lath like grains located between adjacent ferrite grains are martensite and austenite grains, respectively. This indicates that during the deformation process, the block like RA undergoes martensitic transformation first, but the RA with high stability was retained. This further indicated that there was a sustainable TRIP effect for the experimental steel, which can improve its mechanical properties.

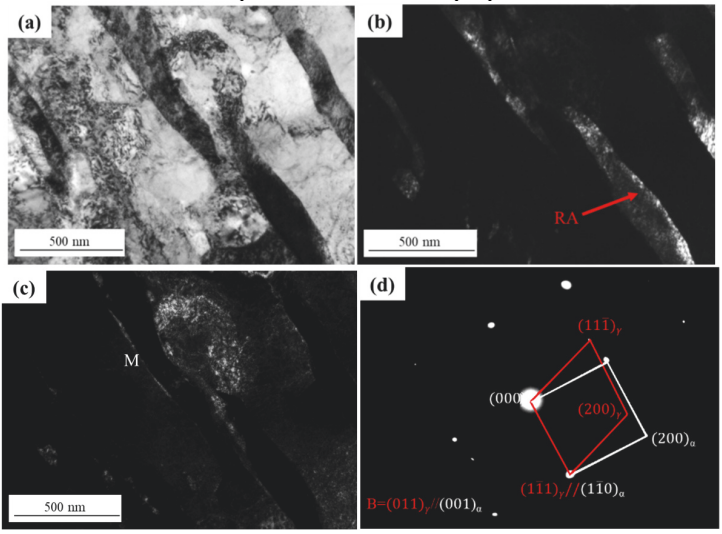

Fig. 12. TEM images of B steel (0.04V) after tensile deformation: (a) bright field image; (b) dark-field TEM image of RA; (c) dark-field TEM image of martensite; (d) SAED pattern

3.2. *Effect of intercritical annealing temperature on mechanical properties of Al-bearing medium Mn steel*

3.2.1. *Microstructure*

Fig. 13 showed the RA content, and carbon content of experimental steel B after IA at 710 ℃, 730 ℃, 750 ℃, and 770 ℃, respectively. After IA at 710-770 ℃, as the IA temperature increased, the RA content first increased and then decreased. When the IA temperature was 730 ℃, the RA content reached a peak of 23.3%. This was because as the IA temperature increased, the austenite fraction increased, but the carbon and alloy element content in per unit austenite decreased, leading to a decreased in austenite thermal stability. During the cooling process, some austenite undergoes martensitic transformation, resulting in a decrease in RA content. When the IA temperature was 770 ℃, the carbon content of austenite was relatively low, leading to a decreased in austenite thermal stability. During the water cooling process, a large amount of austenite undergoes phase transformation. Although it can improve strength, the plasticity also decreases significantly. Therefore, the fine structure of the 770 ℃ IA steel would no longer be tested and analyzed.

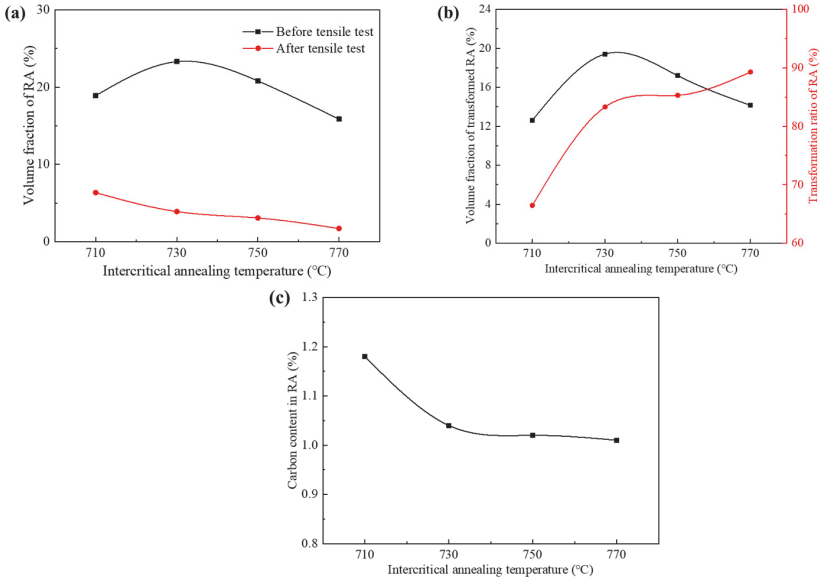

Fig. 13. The RA volume fraction and carbon content of experimental steel treated at different IA temperatures in different two-phase zones: (a) RA volume fraction before and after tensile deformation; (b) The transformation amount and conversion rate of RA; (c) carbon content in RA before tensile deformation

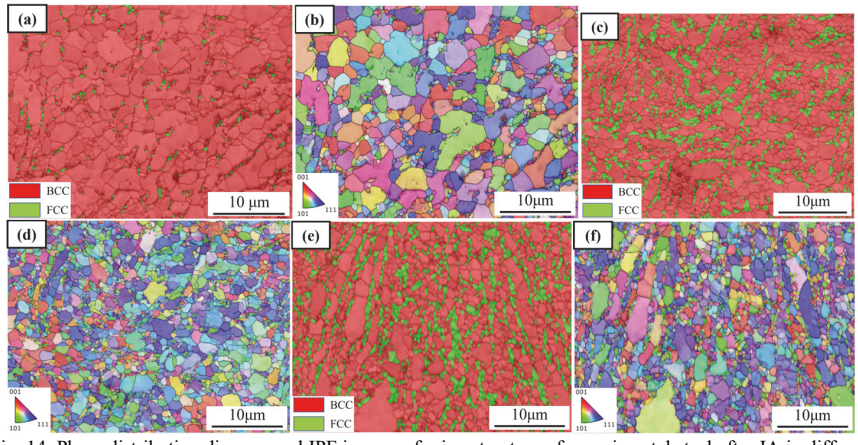

Fig. 14. Phase distribution diagram and IPF images of microstructure of experimental steel after IA in different temperature: (a, b) 710 °C; (c, d) 730 °C; (e, f) 750 °C

Figure 14 shows the phase distribution and IPF images of the experimental steel after being subjected to IA temperatures at 710 °C, 730 °C, and 750 °C. When the IA temperature was 710 °C, the blocky austenite with smaller grain size appears at the phase interface of ferrite, and the blocky austenite with smaller grain size was connected one by one to shown a lath like structure. In addition, a small amount of blocky austenite with smaller grain size can also be observed at the trigeminal grain boundary of ferrite; When the critical IA

temperature rase to 730 ℃, the austenite content becomes more, the grains become coarser, and the lath like structure was more obvious; When the IA temperature increased to 750 ℃, the austenite grains further coarsen. In addition, it can be seen from the reverse pole diagram that the orientation of each austenite grain connected to the banded structure is similar, indicating that austenite nucleates in martensite lath.

3.2.2. *Mechanical properties*

Figure 15 showed the engineering stress-strain curves of experimental steel after IA in different temperatures. It can be seen that as the IA temperature increased, the yield strength first decreased and then increased, and the tensile strength gradually increased. The elongation after fracture and the product of strength and elongation (PSE) both show a trend of increasing first and then decreasing. When the IA temperature was 730 ℃, the experimental steel obtained the highest elongation after fracture (34.0%) and PSE (33.3GPa ·%).

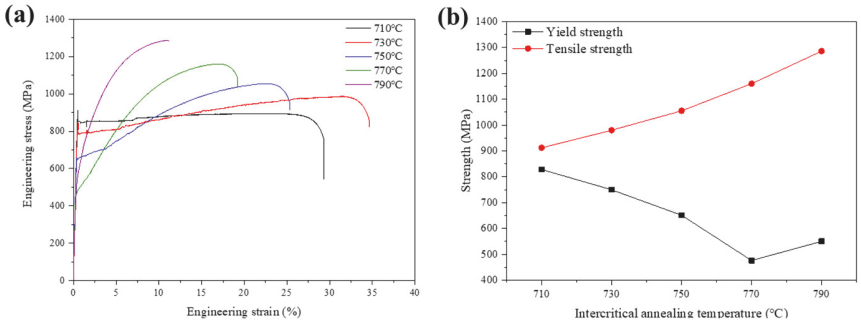

Fig. 15. Engineering stress-strain curve of the experimental steel with different IA temperature （a）Engineering stress-strain curves （b）yield strength and Tensile strength

Experimental steel's tensile strength increased gradually with rising IA temperature due to microstructure evolution and TRIP effect during deformation. At low IA temperature (710 ℃), high austenite thermal stability allowed retention at room temperature but limited TRIP effects due to RA's high mechanical stability, resulting in the lowest tensile strength. At high IA temperature (770 ℃), lower austenite thermal stability led to martensitic transformation, increasing martensite content, decreasing RA content significantly. Lower carbon content and larger grain size reduced RA's mechanical stability. High tensile strength resulted from extensive RA martensitic transformation during deformation.

With rising IA temperature, experimental steel's elongation initially increased and then decreased. Higher RA content amplified the TRIP effect, enhancing steel elongation. RA content variations during in-situ tensile testing post-IA at different temperatures were examined, as depicted in Fig. 16. The RA content in experimental steels decreased with increasing strain post different IA, notably dropping significantly after the yield point. This observation directly validates the RA transformation to martensite, highlighting the TRIP effect in the tensile deformation process.

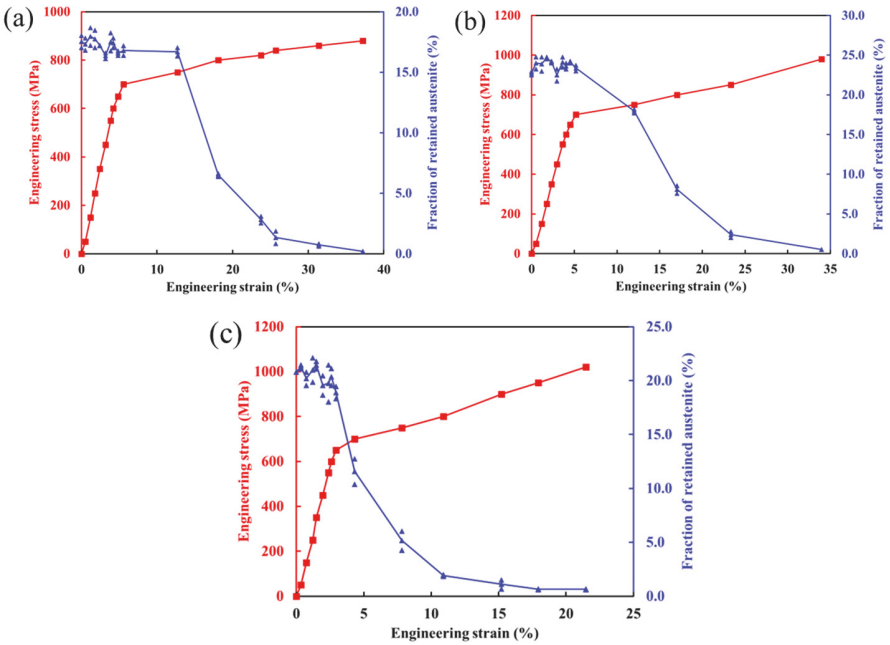

Fig. 16. Changes in RA content with stress-strain curve during in-situ tensile process of experimental steels after IA in different temperatures: (a) 710 °C; (b) 730 °C; (c) 750 °C

4. Conclusions

(1) Observation of experimental steel microstructures post IA revealed banded δ-F, α-F, martensite, and RA with varying vanadium contents. Analysis showed lath-like and block RA with around 400 nm grain sizes, ensuring austenite stability and sustained TRIP effect during deformation. B steel (0.04wt.% V) had the highest carbon content in RA due to aluminum promoting carbon content and vanadium carbide dissolution.

(2) Statistical analysis of vanadium carbide particle size showed dissolution in B steel (0.04 wt.% V) during IA, slight dissolution in C steel (0.08 wt.% V), and no dissolution in D steel (0.13 wt.% V). Optimal vanadium and manganese amounts were needed for carbide dissolution, as increasing vanadium alone did not achieve this, leading to higher carbon content in RA.

(3) Experimental steel densities were below 7.65g/cm3, with fracture elongation exceeding 30% and strength plastic product over 30GPa·%. B steel (0.04wt.% V) outperformed others with tensile strength of 1020MPa and 37.0% elongation, attributed to vanadium enhancing grain boundary and precipitation strengthening. Plasticization mainly stemmed from TRIP effect, with B steel showing highest RA stability and varied form sizes for sustained TRIP effect.

(4) Post IA at 710-770 °C, microstructures comprised banded δ-F, α-F, martensite, and RA. Lower IA temperatures (710 °C) exhibited mainly lamellar and equiaxed RA shapes, transitioning to decreased layered and increased equiaxed structures at higher temperatures.

RA content peaked at 23.3% at 730 ℃ IA temperature. Yield strength varied with IA temperature, while tensile strength increased. Elongation after fracture and PSE initially increased and then decreased, with maximum TEL (34.0%) and PSE (33.3GPa%) at 730 ℃ IA temperature.

References

1. Kang Y. Lightweight vehicle, advanced high strength steel and energy-saving and emission reduction. *Iron & Steel*, **43**,6(2008).
2. Kim H, Suh DW, Kim NJ. Fe-Al-Mn-C lightweight structural alloys: a review on the microstructures and mechanical properties. *Sci Tech Adv Mater*, 14(2013).
3. Woo SD, Kim NJ. Viewpoint set 53: low density steels. *Scripta Mater,* 68(2013).
4. Rana R. Special topic: low density steels. *JOM,* 66(2014).
5. Raabe D, Springer H, Gutierrez-Urrutia I, Roters F, Bausch M, Seol JB, et al. Alloy design, combinatorial synthesis, and microstructure-property relations for low-density Fe-Mn-Al-C austenitic steels. *JOM,* 66(2014).
6. Rana R, Liu C, Ray RK. Evolution of microstructure and mechanical properties during thermomechanical processing of a low-density multiphase steel for automotive application. *Acta Mater,* 75(2014).
7. Sohn SS, Lee BJ, Lee S, Kwak JH. Effect of Mn addition on microstructural modification and cracking behaviour of ferritic light-weight steels. *Metal Mater Trans A,* 45(2014).
8. Yang F, Song R, Li Y, Sun T, Wang K. Tensile deformation of low density duplex Fe-Mn-Al-C steel. *Mater Des,* 76(2015).
9. Zhang L, Song R, Zhao C, Yang F. Work hardening behaviour involving the substructural evolution of an austenite–ferrite Fe–Mn–Al–C steel. *Mater Sci Eng A,* 640(2015).
10. Etienne A, Massardier-Jourdan V, Cazottes S, Garat X, Soler M, Zuazo I, et al. Ferrite effects in Fe-Mn-Al-C triplex steels. *Metal Mater Trans A,* 45(2014).
11. Cai Z, Ding H, Ying Z, Misra RDK. Microstructural evolution and deformation behaviour of a hot-rolled and heat treated Fe-8Mn-4Al-0.2C steel. *J Mater Eng Perform,* 23(2014).
12. Sohn SS, Lee BJ, Lee S, Kim NJ, Kwak JH. Effect of annealing temperature on microstructural modification and tensile properties in 0.35C-3.5Mn-5.8Al lightweight steel. *Acta Mater,* 61(2013).
13. Yang MX, Yuan FP, Xie QG, Wang YD, Ma E, Wu XL. Strain hardening in Fe-16Mn-10Al-0.86C-5Ni high specific strength steel. *Acta Mater,* 109(2016).
14. Yang F, Song R, Li Y, Sun T, Wang K. Tensile deformation of low density duplex Fe-Mn-Al-C steel. *Mater Des,* 76(2015).
15. J. Shi, X.J. Sun, M.Q. Wang, W.J. Hui, H. Dong, W.Q. Cao, Enhanced work-hardening behavior and mechanical properties in ultrafine-grained steels with large-fractioned metastable austenite, *Scr. Mater,* 63 (2010).
16. R.L. Miller, Ultrafine-grained microstructures and mechanical properties of alloy steels, *Metall. Mater. Trans,* **B 3** (1972).
17. Z.H. Cai, H. Ding, R.D.K. Misra, Z.Y. Ying, Austenite stability and deformation behavior in a cold-rolled transformation-induced plasticity steel with medium manganese content, *Acta Mater,* 84 (2015)

18. D.T. Han, Y.B. Xu, R.D. Liu, F. Peng, Y. Zou, W.H. Sun, Improving Mn partitioning and mechanical properties through carbides-enhancing pre-annealing in Mn-reduced transformation-induced plasticity steel, *Scr. Mater,* 187 (2020).
19. Brüx U, Frommeyer G, Jimenez J. Light-weight steels based on iron-aluminium: Influence of micro alloying elements (B, Ti, Nb) on microstructures, textures and mechanical properties. *Steel Res Int,* 73(2012).
20. N. Zhao, M.L. Ding, L. Lin, Y.L. He, J.X. Wang, R.K. Zhang, Y. Zhang, R.D. Liu, L.H. Wang, L. Li, Insights into the relationship between γ/α transformation and strength-ductility of auto-steel with 980 MPa grade based on experiments and theoretical calculations, *Vacuum,* 215 (2023).
21. Z. Li, D. Wu, Effects of hot deformation and subsequent austempering on the mechanical properties of Si-Mn TRIP steels. *Journal of Iron and Steel Research, International,* **46**(2006).
22. N.H. van Dijk, A.M. Butt, L. Zhao, J. Sietsma, S.E. Offerman, J.P. Wright, S. van der Zwaag, Thermal stability of retained austenite in TRIP steels studied by synchrotron X-ray diffraction during cooling, *Acta Mater,* 53(2005).
23. Seo CH, Kwon KH, Choi K, Kim KH, Kwak JH, Leed S, et al. Deformation behaviour of ferrite–austenite duplex lightweight Fe-Mn-Al-C steel. *Scripta Mater,* 66(2012).
24. Sohn SS, Song H, Kim JG, Kwak JH, Kim HS, Lee S. Effects of annealing treatment prior to cold rolling on delayed fracture properties in ferrite-austenite duplex lightweight steels. *Metall Mater Trans A,* 47(2015).
25. Seol JB, Raabe D, Choi P, Park HS, Kwak JH, Park CG. Direct evidence for the formation of ordered carbides in a ferrite-based low-density Fe-Mn-Al-C alloy studied by transmission electron microscopy and atom probe tomography. *Scripta Mater,* 68(2013).